Infrared Radiative Transfer in Finite Cloud Layers

KUO-NAN LIOU AND SZU-CHENG OU

Department of Meteorology, University of Utah, Salt Lake City 84112

(Manuscript received 3 November 1978, in final form 17 May 1979)

ABSTRACT

Analytic solutions to the three-dimensional infrared radiative transfer equation for an anisotropic and isothermal scattering cloud layer are derived by utilizing the four-term truncated spherical harmonics expansion for the scattering phase function and intensity. Computational results of the upward and downward intensity and flux density for cubic, rectangular and plane-parallel clouds employing a wavelength of 10 μm are presented and physically discussed. We show that the emissivities of cubic clouds are ~20–30% lower than the values calculated from the plane-parallel program, and that optically thick cubic clouds cannot be considered as black clouds. Further, we found that cubic clouds undergo much stronger cooling at the top as compared to plane-parallel clouds. Relatively small cooling is also evidenced near the cubic cloud bottom. These computational results and physical findings appear to have significant implications to the interpretation of satellite soundings to infer the cloud-top temperatures of cumulus clouds and to the understanding of infrared cooling in cumulus cloudy atmospheres.

1. Introduction

The popular radiative transfer theory developed for the last three decades (see, e.g., Chandrasekhar, 1950) has been based on the approximation that the scattering layer is assumed to be infinite in the horizontal direction, the so called plane-parallel approximation. In the earth's atmosphere, however, clouds of convective nature normally assume finite horizontal geometries which require the consideration of the transfer processes in multidimensional space. Determinations of the radiative properties of finite clouds have been topics of recent concern in conjunction with the interpretation of satellite radiance observations from cloudy atmospheres (Reynolds *et al.*, 1978), the quantitative understanding of the reflection, transmission and absorption of solar radiation by cloud layers (Liou, 1976), and the conversion of radiance measurements to flux forms in the satellite radiation budget experiment.

Effects of horizontally finite clouds on scattered radiation have been investigated by McKee and Cox (1976) by means of the Monte Carlo method. Theoretical approaches to the problem have also been undertaken by Weinman and Swarztrauber (1968) and more recently by Davies (1978) to study the radiative characteristics of finite clouds in the visible region. Weinman and Davies (1978) have also employed a finite cloud model in the microwave spectrum to understand the effect of the horizontal finiteness on brightness temperature measurements. Radiative transfer in multi-dimensional space has been a subject of extensive research in the field of neutron transport (Case and Zweifel, 1967; Greenspan *et al.*, 1968).

In this paper we investigate the effect of finite clouds on the transfer of infrared radiation. We present in Section 2 the basic formulation of the transfer problem and assumptions utilized in the analyses. In Section 3 the solution of the simplified transfer equation is given on the basis of a four-term spherical-harmonics expansion for the phase function and intensity. Computational results involving the intensity, flux density as well as the emissivity and infrared cooling rate for finite clouds at 10 μm wavelength are presented in Section 4. Physical interpretations of the resulting calculations for various cloud models and comparisons with results derived from the plane-parallel program are carried out.

2. Basic radiative transfer equations and boundary conditions

The basic steady-state thermal infrared radiative transfer equation for homogeneous medium can be written as

$$-\sigma^{-1}(\Omega\cdot\nabla)I(s,\Omega) = I(s,\Omega) - (\tilde{\omega}_\nu/4\pi) \times \int_{4\pi} I(s,\Omega')P(\Omega,\Omega')d\Omega' - (1-\tilde{\omega}_\nu)B_\nu[T(s)], \quad (1)$$

0022-4928/79/101985-12$07.00

where I denotes the monochromatic intensity of the scattered radiation, σ the extinction coefficient, $\mathbf{\Omega}$ is a unit vector specifying the direction of scattering through a position vector $\mathbf{s}$, $\tilde{\omega}_\nu$ denotes the single scattering albedo and $B_\nu(T)$ the Planck function of temperature T. The normalized scattering phase function is defined such that

$$(1/4\pi)\int_{4\pi} P(\mathbf{\Omega},\mathbf{\Omega}')d\Omega = 1. \tag{2}$$

Note that in a homogeneous medium, it is assumed that the scattering parameter σ, $\tilde{\omega}_\nu$ and P are independent of the position vector $\mathbf{s}$. Moreover, the second and third terms on the right-hand side of (1) represent the multiple-scattering and emission contributions, respectively, from a homogeneous medium. These contributions depend on the magnitude of the single-scattering albedo $\tilde{\omega}_\nu$ as evident from Eq. (1). In Cartesian coordinates, the fundamental transfer equation shown in Eq. (1) can be expressed in the form

$$-\sigma^{-1}\left[(1-\mu^2)^{1/2}\cos\phi\frac{\partial}{\partial x}+(1-\mu^2)^{1/2}\sin\phi\frac{\partial}{\partial y}+\mu\frac{\partial}{\partial z}\right]I(x,y,z;\mu,\phi)$$
$$= I(x,y,z;\mu,\phi) - (\tilde{\omega}_\nu/4\pi)\int_0^{2\pi}\int_{-1}^{1} I(x,y,z;\mu',\phi')P(\mu,\phi;\mu',\phi')d\mu'd\phi' - (1-\tilde{\omega}_\nu)B_\nu[T(x,y,z)], \tag{3}$$

where μ denotes the cosine of the emergent angle θ and ϕ the azimuthal angle.

We introduce the spherical-harmonics expansion for the scattering phase function and intensity, respectively, in the form (Case and Zweifel, 1967; Greenspan *et al.*, 1968)

$$P(\mu,\phi;\mu',\phi') = \sum_{n=0}^{N}\sum_{m=-n}^{n}\frac{\tilde{\omega}_n}{2n+1}Y_n^m(\mu,\phi)Y_n^{m*}(\mu',\phi'), \tag{4}$$

$$I(x,y,z;\mu,\phi) = \sum_{n=0}^{N}\sum_{m=-n}^{n}\sqrt{2n+1}I_n^m(x,y,z)Y_n^m(\mu,\phi), \tag{5}$$

where N is the total number of terms, the asterisk denotes the complex conjugate, $\tilde{\omega}_n$'s are coefficients of the expansion ($\tilde{\omega}_0 = 1$) and the spherical harmonics are defined by

$$Y_n^m(\mu,\phi) = \left[(2n+1)\frac{(n-|m|)!}{(n+|m|)!}\right]^{1/2}(-1)^{(m+|m|)/2}P_n^{|m|}(\mu)e^{im\phi}, \tag{6}$$

where $P_n^m(\mu)$ represents the associated Legendre polynomials and $|m|$ denotes the absolute value of m. The spherical harmonics are normalized in such way that

$$(1/4\pi)\int_0^{2\pi}\int_{-1}^{1} Y_n^m(\mu,\phi)Y_l^{k*}(\mu,\phi)d\mu d\phi = \delta_n^l\delta_m^k, \tag{7}$$

where δ_n^l and δ_m^k are Kronecker delta functions which are equal to 1 when $l = n$ and $k = m$, and zero, otherwise.

Substituting Eqs. (4) and (5) into Eq. (3) and successively carrying out the integration operations

$$\int_0^{2\pi}\int_{-1}^{1} Y_l^{k*}(\mu,\phi)\times[\text{Eq. (3)}]d\mu d\phi, \qquad l = 0, 1, \cdots, N; \qquad k = -l, \cdots, l,$$

yields a set of partial differential equations

$$[(l-k+1)(l+k+1)]^{1/2}\frac{\partial}{\partial z}I_{l+1}^k + [(l-k)(l+k)]^{1/2}\frac{\partial}{\partial z}I_{l-1}^k$$
$$-\frac{1}{2}\left(\frac{\partial}{\partial x}-i\frac{\partial}{\partial y}\right)\{[(l+k)(l+k-1)]^{1/2}I_{l-1}^{k-1} - [(l-k+2)(l-k+1)]^{1/2}I_{l+1}^{k-1}\}$$
$$-\frac{1}{2}\left(\frac{\partial}{\partial x}+i\frac{\partial}{\partial y}\right)\{[(l+k+1)(l+k+2)]^{1/2}I_{l+1}^{k+1} - [(l-k-1)(l-k)]^{1/2}I_{l-1}^{k+1}$$
$$= (2l+1)\sigma\{-I_l^k[1-\tilde{\omega}_\nu\tilde{\omega}_l/(2l+1)] + \delta_0^k\delta_0^l B_\nu(T)(1-\tilde{\omega}_\nu)/(2l+1)\}, \tag{8}$$

where $\delta_0^{k(l)}$ is equal to 1 when $k(l) = 0$, and equal to zero when $k(l) \neq 0$. We note here that in the process of algebraic analyses, the recursion formulas for $(1 - \mu^2)^{1/2} \cos\phi Y_n^m(\mu,\phi)$, $(1 - \mu^2)^{1/2} \sin\phi Y_n^m(\mu,\phi)$ and $\mu Y_n^m(\mu,\phi)$ were used. Eq. (8) consists of $(2l + 1)$ modes for $l = 0, 1, \cdots, N$. In this study we select the zero and first modes and set $l = 2, \cdots, N$ modes to zero to obtain the following four basic equations:

$$\frac{\partial I_1^0}{\partial \tau_z} + \frac{1}{\sqrt{2}}\left(\frac{\partial}{\partial \tau_x} - i\frac{\partial}{\partial \tau_y}\right) I_1^{-1} - \frac{1}{\sqrt{2}}\left(\frac{\partial}{\partial \tau_x} + i\frac{\partial}{\partial \tau_y}\right) I_1^1 = -(1 - \tilde{\omega}_\nu)[I_0^0 - B_\nu(T)], \tag{9}$$

$$(1 - \tilde{\omega}_\nu \tilde{\omega}_1/3) I_1^{-1} = \frac{-1}{3\sqrt{2}}\left(\frac{\partial}{\partial \tau_x} + i\frac{\partial}{\partial \tau_y}\right) I_0^0, \tag{10}$$

$$(1 - \tilde{\omega}_\nu \tilde{\omega}_1/3) I_1^0 = \frac{-1}{3}\frac{\partial I_0^0}{\partial \tau_z}, \tag{11}$$

$$(1 - \tilde{\omega}_\nu \tilde{\omega}_1/3) I_1^1 = \frac{1}{3\sqrt{2}}\left(\frac{\partial}{\partial \tau_x} - i\frac{\partial}{\partial \tau_y}\right) I_0^0. \tag{12}$$

In these equations the optical depths in the X, Y and Z directions are defined by $\tau_x = \sigma x$, $\tau_y = \sigma y$ and $\tau_z = \sigma z$. Substitution of the expressions I_1^1, I_1^0 and I_1^{-1} in Eqs. (10)–(12) into Eq. (9) yields

$$\nabla_\tau^2 I_0^0 = \eta^2 [I_0^0 - B_\nu(T)], \tag{13}$$

where the Laplace operator $\nabla_\tau^2 = \partial^2/\partial^2\tau_x + \partial^2/\partial^2\tau_y + \partial^2/\partial^2\tau_z$, and

$$\eta^2 = 3(1 - \tilde{\omega}_\nu)(1 - g\tilde{\omega}_\nu). \tag{14}$$

Here the asymmetry factor g is defined as $\tilde{\omega}_1/3$. Eq. (13) represents the well-known Poisson (or diffusion) equation whose solution can be derived subject to the radiation boundary conditions imposed.

Let a, b and c be optical depths in the τ_z, τ_y and τ_x directions, respectively. Consider an isolated rectangular shaped cloud with an isothermal temperature T_c above a black surface whose temperature is T_s and assume that there is no atmospheric contribution for simplicity. Thus, there will be no downward flux density at the cloud top, whereas the upward flux density reaching the cloud base is simply equal to $\pi B_\nu(T_s)$. Moreover, each vertical side wall of the finite cloud receives only half of the emitted flux density from the surface, i.e., $\pi B_\nu(T_s)/2$, since the emission from the surface is in all directions. It follows that the radiation boundary conditions in terms of the flux density for the finite cloud for the top and bottom surfaces may be expressed by

$$\left.\begin{aligned} F^{\downarrow}(\tau_x,\tau_y,0) &= \int_0^{2\pi}\int_0^1 I(\tau_x,\tau_y,0;\ \mu,\phi)\mu d\mu d\phi = 0 \\ F^{\uparrow}(\tau_x,\tau_y,a) &= \int_0^{2\pi}\int_0^1 I(\tau_x,\ \tau_y,\ a;\ -\mu,\ \phi)\mu d\mu d\phi = \pi B_\nu(T_s) \end{aligned}\right\}. \tag{15}$$

For the surfaces in the τ_y direction, they are given by

$$\left.\begin{aligned} F^{\leftarrow}(\tau_x,0,\tau_z) &= \int_0^{\pi}\int_{-1}^1 I(\tau_x,0,\tau_z;\ \mu,\phi)(1 - \mu^2)^{1/2} \sin\phi d\mu d\phi = \pi B_\nu(T_s)/2 \\ F^{\rightarrow}(\tau_x,b,\tau_z) &= \int_{\pi}^{2\pi}\int_{-1}^1 I(\tau_x,b,\tau_z;\ \mu,\phi)(1 - \mu^2)^{1/2} \sin\phi d\mu d\phi = \pi B_\nu(T_s)/2 \end{aligned}\right\}. \tag{16}$$

Moreover, for the surfaces in the τ_x direction, we have

$$\left.\begin{aligned} F^{\leftarrow}(0,\tau_y,\tau_z) &= \int_{-\pi/2}^{\pi/2}\int_{-1}^1 I(0,\tau_y,\tau_z;\ \mu,\phi)(1 - \mu^2)^{1/2} \cos\phi d\mu d\phi = \pi B_\nu(T_s)/2 \\ F^{\rightarrow}(c,\tau_y,\tau_z) &= \int_{\pi/2}^{3\pi/2}\int_{-1}^1 I(c,\tau_y,\tau_z;\ \mu,\phi)(1 - \mu^2)^{1/2} \cos\phi d\mu d\phi = \pi B_\nu(T_s)/2 \end{aligned}\right\}. \tag{17}$$

Inserting the truncated spherical-harmonics expansion for the intensity into Eqs. (15)–(17), and making use of Eqs. (10)–(12), the radiation boundary conditions may be derived in terms of I_0^0. In the τ_z direction, we obtain

$$\left.\begin{aligned}\left(\frac{\partial I_0^0}{\partial \tau_z}\right)_{\tau_z=0} - hI_0^0(\tau_x,\tau_y,0) &= 0\\ \left(\frac{\partial I_0^0}{\partial \tau_z}\right)_{\tau_z=a} + hI_0^0(\tau_x,\tau_y,a) &= hB_\nu(T_s)\end{aligned}\right\}. \quad (18)$$

In the τ_y direction, Eq. (16) can be simplified to give

$$\left.\begin{aligned}\left(\frac{\partial I_0^0}{\partial \tau_y}\right)_{\tau_y=0} - hI_0^0(\tau_x,0,\tau_z) &= -hB_\nu(T_s)/2\\ \left(\frac{\partial I_0^0}{\partial \tau_y}\right)_{\tau_y=b} + hI_0^0(\tau_x,b,\tau_z) &= hB_\nu(T_s)/2\end{aligned}\right\}, \quad (19)$$

and in the τ_x direction the radiation boundary conditions are given by

$$\left.\begin{aligned}\left(\frac{\partial I_0^0}{\partial \tau_x}\right)_{\tau_x=0} - hI_0^0(0,\tau_y,\tau_z) &= -hB_\nu(T_s)/2\\ \left(\frac{\partial I_0^0}{\partial \tau_x}\right)_{\tau_x=c} + hI_0^0(c,\tau_y,\tau_z) &= hB_\nu(T_s)/2\end{aligned}\right\}. \quad (20)$$

In Eqs. (18)–(20), $h = \frac{3}{2}(1 - g\tilde{\omega}_\nu)$. The Poisson equation involving I_0^0 may now be solved by utilizing the boundary conditions denoted in Eqs. (18)–(20). Subsequently, I_1^1, I_1^0 and I_1^{-1} may be determined from Eqs. (10)–(12).

3. Solution of the transfer equation

For the convenience of the following analyses and calculations, we define

$$\tilde{I} = I_0^0 - B_\nu(T_s)/2, \quad (21)$$

and let

$$\tilde{B} = B_\nu(T_s)/2 - B_\nu(T_c). \quad (22)$$

As will be seen below the transformation of variable in Eq. (21) allows the reduction of the number of inhomogeneous boundary conditions from five to two. Hence, Eq. (13) may be rewritten as

$$\nabla_\tau^2 \tilde{I} = \eta^2(\tilde{I} + \tilde{B}). \quad (23)$$

On the basis of these definitions the radiation boundary conditions given by Eqs. (18)–(20) may be rewritten in the forms

$$\left.\begin{aligned}\left(\frac{\partial \tilde{I}}{\partial \tau_z}\right)_{\tau_z=0} - h\tilde{I}(\tau_x,\tau_y,0) &= hB_\nu(T_s)/2\\ \left(\frac{\partial \tilde{I}}{\partial \tau_z}\right)_{\tau_z=a} + h\tilde{I}(\tau_x,\tau_y,a) &= hB_\nu(T_s)/2\end{aligned}\right\}, \quad (24)$$

$$\left.\begin{aligned}\left(\frac{\partial \tilde{I}}{\partial \tau_y}\right)_{\tau_y=0} - h\tilde{I}(\tau_x,0,\tau_z) &= 0\\ \left(\frac{\partial \tilde{I}}{\partial \tau_y}\right)_{\tau_y=b} + h\tilde{I}(\tau_x,b,\tau_z) &= 0\end{aligned}\right\}, \quad (25)$$

$$\left.\begin{aligned}\left(\frac{\partial \tilde{I}}{\partial \tau_x}\right)_{\tau_x=0} - h\tilde{I}(0,\tau_y,\tau_z) &= 0\\ \left(\frac{\partial \tilde{I}}{\partial \tau_x}\right)_{\tau_x=c} + h\tilde{I}(c,\tau_y,\tau_z) &= 0\end{aligned}\right\}. \quad (26)$$

Weinman and Davies (1978) have presented a similar set of radiation boundary conditions for microwave radiation in which the emissivity of the surface is considered to be less than unity.

Inspection of the above partial differential equations reveals that separation of variables may be applicable. Following the procedures outlined by Berg and McGregor (1966) for the inhomogeneous problem, we let

$$\tilde{I} = X(\tau_x)Y(\tau_y)Z(\tau_z), \quad (27)$$

so that the related homogeneous problems lead to the ordinary differential equations

$$\left.\begin{aligned}&\frac{d^2X}{d\tau_x^2} + \lambda_n^2 X = 0\\ &\text{with boundary conditions}\\ &X'(0) - hX(0) = 0\\ &X'(c) + hX(c) = 0\end{aligned}\right\}, \quad (28)$$

$$\left.\begin{aligned}&\frac{d^2Y}{d\tau_y^2} + \lambda_m^2 Y = 0\\ &\text{with boundary conditions}\\ &Y'(0) - hY(0) = 0\\ &Y'(b) + hY(b) = 0\end{aligned}\right\}, \quad (29)$$

where λ_n and λ_m represent the eigenvalues in the τ_x and τ_y directions, respectively. By means of the elementary methods (see, e.g., Berg and McGregor, 1966) the eigensolutions of these two sets of ordinary differential equations are given, respectively, by

$$\left.\begin{aligned}X_n(\tau_x) &= \cos(\lambda_n\tau_x) + \frac{h}{\lambda_n}\sin(\lambda_n\tau_x)\\ Y_m(\tau_y) &= \cos(\lambda_m\tau_y) + \frac{h}{\lambda_m}\sin(\lambda_m\tau_y)\end{aligned}\right\}. \quad (30)$$

Moreover, the corresponding eigenvalues of the solutions can be determined from

$$2\cot\lambda_l\left(\frac{c}{b}\right) = \left(\frac{\lambda_l}{h} - \frac{h}{\lambda_l}\right), \quad \begin{matrix} l = n \text{ or } m,\\ l = 1, 2, \ldots. \end{matrix} \quad (31)$$

By virtue of the principle of superposition, we have

$$\tilde{I}(\tau_x,\tau_y,\tau_z) = \sum_{n=1}^{\infty}\sum_{m=1}^{\infty} X_n(\tau_x)Y_m(\tau_y)Z_{nm}(\tau_z). \quad (32)$$

To determine the function Z_{nm}, we first utilize the orthogonal properties of X_n and Y_m and differentiate Z_{nm} with respect to τ_z to obtain

$$\frac{d^2Z_{nm}}{d\tau_z^2} = \zeta_{nm}^2 Z_{nm} + t_{nm}, \quad (33)$$

where

$$\zeta_{nm}^2 = \lambda_n^2 + \lambda_m^2 + \eta^2, \quad (34)$$

$$\left.\begin{aligned} t_{nm} &= \frac{\eta^2\tilde{B}}{f_n g_m}\int_0^b\int_0^c X_n Y_m d\tau_x d\tau_y \\ f_n &= \int_0^c X_n^2 d\tau_x, \quad g_m = \int_0^b Y_m^2 d\tau_y \end{aligned}\right\}. \quad (35)$$

It is clear that the solution of Eq. (33) is simply

$$Z_{nm}(\tau_z) = C_+e^{\zeta_{nm}\tau_z} + C_-e^{-\zeta_{nm}\tau_z} - t_{nm}/\zeta_{nm}^2. \quad (36)$$

The unknown coefficients C_+ and C_- can be determined through the use of the radiation boundary conditions denoted in Eq. (24). They are given by

$$C_+ = \frac{h}{\Delta_{nm}}\left[\left(\frac{s_{nm}}{f_n g_m} + \frac{t_{nm}}{\zeta_{nm}^2}\right)(\zeta_{nm} + h) - \left(\frac{s_{nm}}{f_n g_m} - \frac{t_{nm}}{\zeta_{nm}^2}\right)(\zeta_{nm} - h)e^{-\zeta_{nm}a}\right], \quad (37)$$

$$C_- = \frac{h}{\Delta_{nm}}\left[\left(\frac{s_{nm}}{f_n g_m} + \frac{t_{nm}}{\zeta_{nm}^2}\right)(\zeta_{nm} - h) - \left(\frac{s_{nm}}{f_n g_m} - \frac{t_{nm}}{\zeta_{nm}^2}\right)(\zeta_{nm} + h)e^{\zeta_{nm}a}\right], \quad (38)$$

where

$$s_{nm} = \tfrac{1}{2}B_\nu(T_s)\int_0^c\int_0^b X_n Y_m d\tau_y d\tau_x, \quad (39)$$

$$\Delta_{nm} = \begin{vmatrix} (\zeta_{nm} - h) & -(\zeta_{nm} + h) \\ (\zeta_{nm} + h)e^{\zeta_{nm}a} & -(\zeta_{nm} - h)e^{-\zeta_{nm}a} \end{vmatrix}. \quad (40)$$

Thus, the complete solution for Eq. (23) in terms of I_0^0 is

$$I_0^0(\tau_x,\tau_y,\tau_z) = \sum_{n=1}^{\infty}\sum_{m=1}^{\infty}(C_+e^{\zeta_{nm}\tau_z} + C_-e^{-\zeta_{nm}\tau_z} - t_{nm}/\zeta_{nm}^2)X_n(\tau_x)Y_m(\tau_y) + B_\nu(T_s)/2 \quad (41)$$

and the truncated intensity may be written in the form

$$I(\tau_x,\tau_y,\tau_z;\mu,\phi) = I_0^0 - \frac{3}{2h}(1-\mu^2)^{1/2}\left(\frac{\partial I_0^0}{\partial\tau_x}\cos\phi + \frac{\partial I_0^0}{\partial\tau_y}\sin\phi\right) - \frac{3}{2h}\mu\frac{\partial I_0^0}{\partial\tau_z}. \quad (42)$$

Moreover, the upward and downward flux densities are given, respectively, by the expressions

$$\left.\begin{aligned} F^{\uparrow}(\tau_x,\tau_y,\tau_z) &= \int_0^{2\pi}\int_{-1}^{0} I(\tau_x,\tau_y,\tau_z;\mu,\phi)\mu d\mu d\phi \\ F^{\downarrow}(\tau_x,\tau_y,\tau_z) &= \int_0^{2\pi}\int_0^{1} I(\tau_x,\tau_y,\tau_z;\mu,\phi)\mu d\mu d\phi \end{aligned}\right\}. \quad (43)$$

In a similar manner, the side flux densities in the τ_x and τ_y directions can also be written. The integrations in the flux density equations can be carried out analytically by substituting the intensity expressions denoted in Eq. (42).

4. Computational results and discussions

In the intensity and flux density calculations reported here we have employed a wavelength of 10 μm and have assumed identical optical depths in the X and Y directions. Mie scattering calculations for a typical cumulus cloud were carried out for the 10 μm wavelength to generate the necessary single-scattering parameters. The single-scattering albedo in this case is 0.63 and the asymmetry factor is ~0.75. It should be noted that absorption by water vapor is not considered in this study. Further, the eigenvalues required in the transfer analyses were calculated from Eq. (31) on the basis of a Newton's iteration method. As evident from Eqs. (41) and (42), the intensity component is proportional to the exponent of the sum of eigenvalues in the τ_x and τ_y directions. Hence, these eigenvalues may be thought of as some sorts of extinction parameters from which the radiation field within the cloud is generated. The meaning of eigenvalues in the solution of the radiative transfer equation has been pointed out previously by Liou (1973).

TABLE 1. Some typical eigenvalues λ_l.

l	τ = 2	τ = 20	τ = 200
1	0.7384	0.1370	0.0155
2	0.3340 × 10	0.4158	0.0464
4	0.9495 × 10	0.1002 × 10	0.1084
8	0.2202 × 10^2	0.2228 × 10	0.2323
16	0.4714 × 10^2	0.4727 × 10	0.4807
32	0.9740 × 10^2	0.9746 × 10	0.9799
64	0.1979 × 10^3	0.1980 × 10^2	0.1982 × 10
128	0.3990 × 10^3	0.3990 × 10^2	0.3991 × 10

The searching of the eigenvalues using the Newton's iteration method begins with the initial guess of $\lambda_l^{(n)}$ $(n = 0)$. The iteration is terminated when $\left|\lambda_l^{(n)}/\lambda_l^{(n-1)} - 1\right| \leq 10^{-25}$. Numerical experiments show that the iteration method utilized for the eigenvalue determination is very efficient for $l \leq 300$. In Table 1, we present some typical eigenvalues using the single-scattering parameters generated from the Mie scattering program described previously. It is evident that the eigenvalue decreases as the optical depth increases and increases rapidly with increasing l.

From Eqs. (41)–(43), it is seen that the resulting intensity and flux density, in principle, depend on an infinite number of eigenfunction expansion. However, in numerical computations, only a finite number of terms is possible and the convergence of the solution has to be tested. We may symbolically express the intensity in the form

$$I = \sum_{n=1}^{N} \sum_{l=1}^{n} Q_{nm}(\tau_x,\tau_y) W_{nm}(\tau_z), \quad m = n - l + 1,$$

where Q_{nm} is associated with the eigenvalues λ_n and λ_m and the horizontal coordinates, W_{nm} is related to ζ_{nm} and the vertical coordinate, and $N(N + 1)/2$ is the total number of terms employed in the numerical computations. Numerical computations are terminated when the convergence test $\left|I^{(N)}/I^{(N-1)} - 1\right| \leq 10^{-5}$ is met. The total number of terms N required relies significantly upon the optical depth utilized in the analysis. For a cloud having optical depth of (1,1,1) only 18 term expansions in N are needed to achieve the convergence everywhere within the cloud. However, for the case of (10,100,100), for instance, we found that about 300 terms in the N expansion are required to meet the convergence criterion. The convergence of the solution also depends in certain degree on the position within the cloud where the intensity or flux density is being evaluated. It was found that near the cloud edge more terms are required in the computations as compared with the central portion of the cloud. In all the resulting computations associated with intensity, flux density, emissivity and infrared cooling rate reported below, the convergence criterion described previously has been tested and achieved.

Fig. 1 illustrates a three-dimensional upwelling intensity distribution ($\mu = -1$) at the top of a finite cloud whose temperature is 0°C illuminated by a black surface having a temperature of 10°C. The cloud optical depths in the three directions are assumed to be 10 and the intensity unit is normalized with respect to $\pi B_\nu(T_s)$. We found that the intensity distribution in the τ_x, τ_y plane of a finite cubic enclosure is symmetric with respect to the two diagonal and dichotomous lines. The upwelling intensity decreases from the edge of the cloud and then increases toward the center of the cloud with a maximum value at the central point. Because of the effective emission contribution from the surface to the side walls of an isolated cubic cloud, the

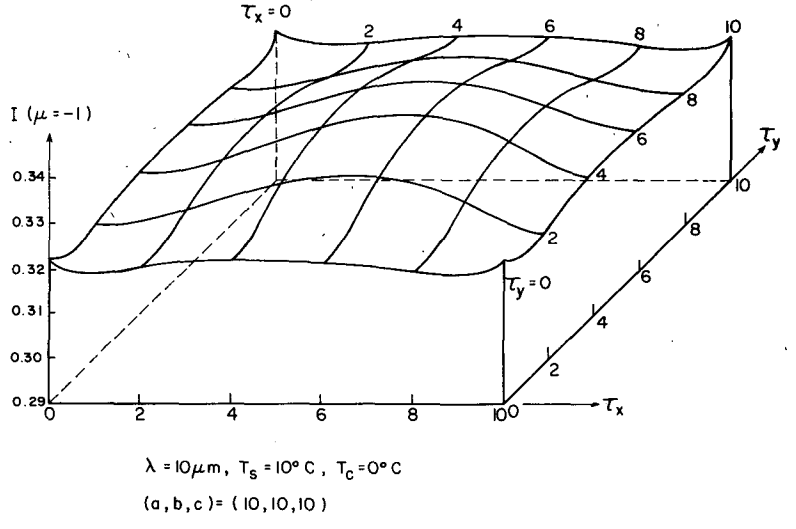

FIG. 1. Three-dimensional upwelling intensity distribution ($\mu = -1$) at the top of a cubic cloud having an optical thickness of 10 in the X, Y and Z directions.

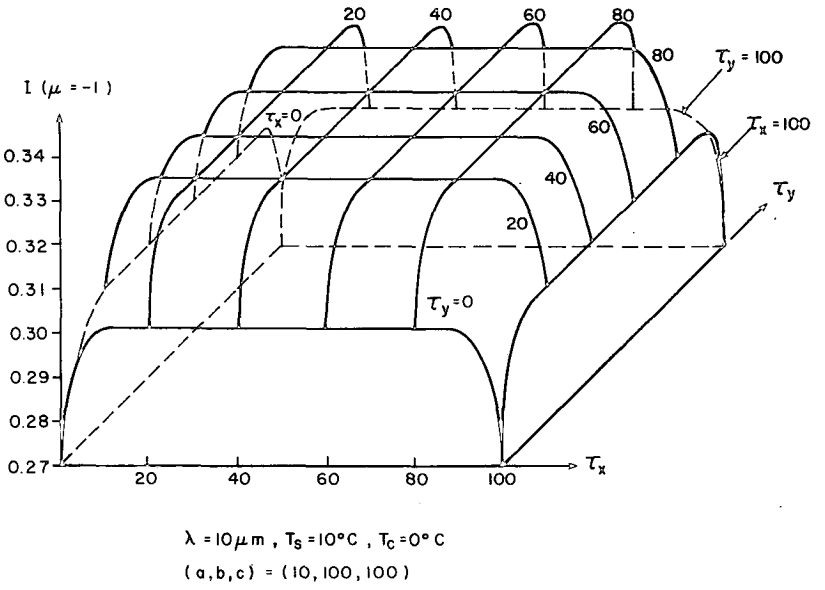

FIG. 2. Three-dimensional upwelling intensity distribution ($\mu = -1$) at the top of a rectangular cloud having optical thicknesses of 100, 100 and 10 in the X, Y and Z directions, respectively.

edges show a larger upwelling intensity. The four corner points produce discontinuous intensity values owing to the inapplicability of the spherical harmonics expansions at these points. Fig. 2 illustrates the upwelling intensity at the top of a rectangular cloud layer having vertical and horizontal optical depths of 10 and 100, respectively. An almost constant upwelling intensity is observed over the region from the optical depth of about 20–80. This value is very close to that computed from the plane-parallel transfer program developed by Liou (1973). In contrast to the cubic cloud, the upwelling intensity decreases from the central portion of a rectangular cloud to the edge. This is because of the effective emission contribution from the surface to the cloud bottom in view of the large horizontal extent considered in the transfer calculations. Clearly, the effect of the cloud finiteness when the horizontal extent is much greater than the vertical dimension is only on the edge of the cloud where the emergent intensity decreases.

As illustrated in Figs. 1 and 2 the emergent intensities depend on the position within the cloud. Thus, from the remote sounding point of view or when the radiative property of the entire cloud is desirable, integration of the intensity distribution over the horizontal plane of the cloud is required. The average intensity at a given horizontal level may be derived from

$$\bar{I}(\tau_z,\mu) = (1/bc)\int_0^b \int_0^c I(\tau_x,\tau_y,\tau_z,\mu)d\tau_x d\tau_y. \quad (44)$$

This integration can be carried out analytically by substituting the intensity expression denoted in Eq. (42). In Fig. 3, we present the average intensity [per units of $\pi B_\nu(T_s)$] emergent from the cloud top ($\tau_z = 0$) as a function of the emergent angle for vertical cloud optical depths of 1 and 10. Comparison

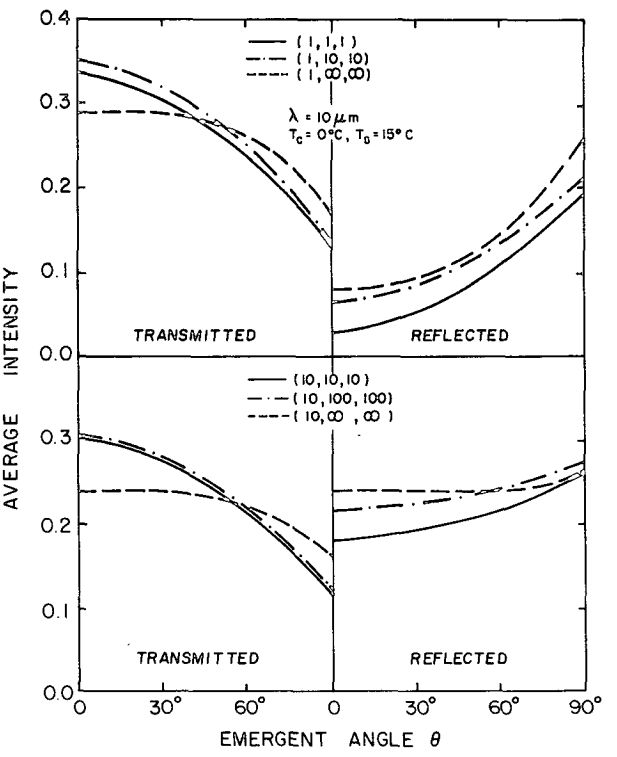

FIG. 3. Averaged reflected (downward) and transmitted (upward) intensities normalized with respect to $\pi B_\nu(T_s)$ as functions of the emergent angle for various cloud models.

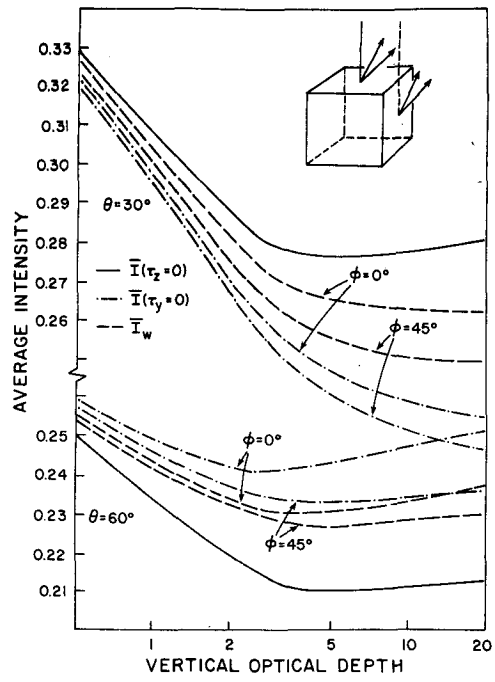

FIG. 4. Averaged emergent intensity from a cubic cloud normalized with respect to $\pi B_\nu(T_s)$ as a function of the optical depth for two zenith angles of 30° and 60°.

of the average transmitted (upward) and reflected (downward) intensity for cubic clouds, rectangular clouds (clouds with much larger horizontal extents) and plane-parallel clouds are carried out. The upward intensities emergent from cubic clouds are smaller than those from rectangular clouds having horizontal extents 10 times greater than the vertical depth. It is also evident that clouds having finite horizontal extents have larger and smaller upward intensities in the upwelling and side directions, respectively, when they are compared with plane-parallel values. Numerical experiments reveal that the larger upwelling intensity from finite clouds is due to the emission contribution from the side walls from which stronger forward scattering in the upwelling directions is generated.

The side walls of a finite cloud also produce scattered intensities in all directions. In conjunction with possible satellite sensing applications, it appears to be significant to present the average upwelling intensity from the side for a cubic cloud. The scattered intensity from the side walls depends not only on the zenith angle, but also on the azimuthal angle. In analogy to Eq. (44) we define the average intensity emergent from the τ_y face in the form

$$\bar{I}(\tau_y;\mu,\phi) = (1/ab)\int_0^a\int_0^b I(\tau_x,\tau_y,\tau_z;\mu,\phi)d\tau_y d\tau_z, \quad (45)$$

where we note that $\mu = \cos\theta$, and θ is the emergent angle with respect to the local zenith defined previously. Similarly, $\bar{I}(\tau_x;\mu,\phi)$ emergent from the τ_x face may be defined. Moreover, with average intensities at the top and sides known, we may also define an area-weighted upwelling intensity emergent from the surface of a finite cloud (i.e., τ_x, τ_y, $\tau_z = 0$) in the form

$$\bar{I}_W(\mu,\phi) = \frac{bc|\mu|\bar{I}(0,\mu) + ab|(1-\mu^2)^{1/2}\cos\phi|\bar{I}(0;\mu,\phi) + ac|(1-\mu^2)^{1/2}\sin\phi|\bar{I}(0;\mu,\phi)}{bc|\mu| + ab|(1-\mu^2)^{1/2}\cos\phi| + ac|(1-\mu^2)^{1/2}\sin\phi|}, \quad (46)$$

where $-1 \leq \mu \leq 1$ and $0 \leq \phi \leq 2\pi$. We found that the emergent intensities are symmetrical in the azimuthal directions from 0 to $\pi/2$ and $\pi/2$ to π.

Shown in Fig. 4 is the upward intensity from a cubic cloud as a function of the optical depth normalized with respect to $\pi B_\nu(T_s)$ for two emergent angles of 30° and 60°. The solid and dashed lines denote the upwelling intensity from the top and side ($\tau_y = 0$), respectively, and the dots represent the area-weighted upwelling intensities. The top curves are for $\theta = 30°$, while the bottom curves are for $\theta = 60°$. For $\theta = 30°$ the upwelling intensity emergent from the side is smaller than that from the top, whereas the reverse is true for $\theta = 60°$. The azimuthal dependence of the upwelling intensity from the side is such that larger values are observed close to the normal plane when $\phi = 0°$. In general, for a given optical depth we found that the emergent intensity has maximum values near the directions normal to the surface of the cubic cloud. In regard to the application of the resulting calculations to sounding of cloud compositions from satellite, information concerning the relative geometrical configuration of the satellite viewing radiometer and the cloud position is needed.

Fig. 5 shows the average upward and downward flux densities for cubic, rectangular and plane-parallel clouds as functions of the vertical optical depth using two cloud temperatures of 10 and −10°C. The equivalent transmitted (upward) and equivalent reflected (downward) flux densities[1] are defined, respectively, by

[1] These quantities contain not only flux density scattered by the cloud but also flux density emitted by the cloud layer. It should be noted that observations of broad-band infrared properties of clouds in the atmosphere contain both the scattered and emitted components, and therefore the theoretical parameters defined here are appropriate when comparisons with observations are desirable.

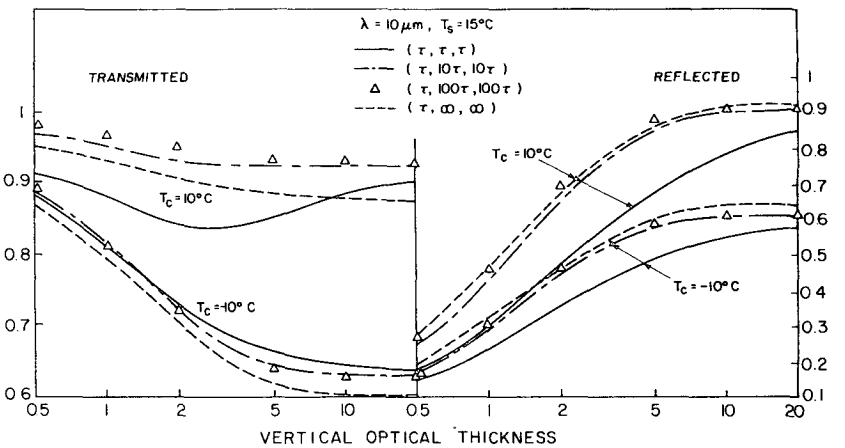

FIG. 5. Averaged reflected (downward) and transmitted (upward) flux densities normalized with respect to $\pi B_\nu(T_s)$ as functions of the vertical optical thickness for various cloud models and cloud temperatures.

$$\left.\begin{aligned} T(a) &= \frac{\bar{F}^{\uparrow}(0)}{\pi B_\nu(T_s)} = \frac{1}{\pi B_\nu(T_s)}\frac{1}{bc}\int_0^b\int_0^c F^{\uparrow}(\tau_x,\tau_y,0)d\tau_x d\tau_y \\ R(a) &= \frac{\bar{F}^{\downarrow}(c)}{\pi B_\nu(T_s)} = \frac{1}{\pi B_\nu(T_s)}\frac{1}{bc}\int_0^b\int_0^c F^{\downarrow}(\tau_x,\tau_y,a)d\tau_x d\tau_y \end{aligned}\right\}. \tag{47}$$

The equivalent reflected (downward) flux densities for various cloud models increase as the vertical optical depth increases in which the cloud temperature shows significant effect. The downward and upward flux densities for cubic clouds are smaller and larger, respectively, as compared to those for rectangular and plane-parallel clouds. For a warm cloud temperature (10°C) the equivalent transmitted (upward) flux densities of the cubic clouds show a minimum at the vertical optical depth of about 3. This behavior is quite different from our general understanding that the cloud transmission decreases as the optical depth increases. Obviously, the finite horizontal extent, and cloud and ground temperatures are significant physical factors which influence the infrared transfer processes. We also note that the upward and downward flux densities of clouds having larger horizontal dimensions match quite closely with the plane-parallel values owing to the fact that the emergent intensities are averaged over all the emergent angles.

In a recent paper by Joseph *et al.* (1976), it has been demonstrated that the inclusion of the forward diffraction peak of the phase function improves the flux calculations for plane-parallel scattering layers. The so-called δ-Eddington approximation involves the scaling of the vertical optical depth, the single-scattering albedo and the asymmetry factor by an appropriate portion of the fractional forward peak in the phase function. Since there is only one optical depth in plane-parallel problems, the adjustment of the scattering parameters may be carried out physically. For radiative transfer in multi-dimensional space, the scaling of the optical depths in three directions is not obvious and the physical foundation for the empirical adjustment has not been established as yet. However, we have carried out the incorporation of the δ-function adjustment equation developed for plane-parallel problems into the three-dimensional flux calculations. Our numerical experiments reveal that the resulting flux computations are exactly the same with and without the δ-function adjustment. In fact, since the flux solution can be expressed in terms of the analytical eigensolution, it can be proven that the solution is invariant with and without the inclusion of the δ-function adjustment. There are some questions regarding the scattering contribution in the thermal infrared region. Because the size of cloud droplets is of the same order as the infrared wavelength the scattering process needs to be taken into account. In general, it depends on the single-scattering albedo, the optical depth of the cloud and the temperature field.

Because the cloud emissivity is a fundamental value in the theory of infrared radiation transfer in the earth's atmosphere, we therefore investigate the finite cloud effect on its behavior. Fig. 6 shows the average emissivity, defined as the ratio of the

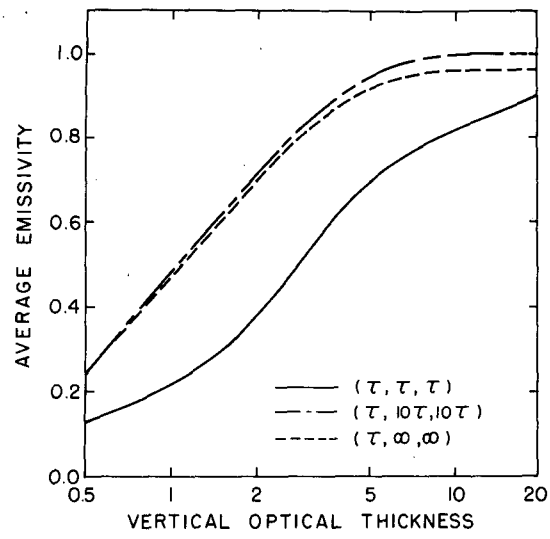

FIG. 6. Cloud emissivity as a function of the vertical optical thickness for various cloud models.

average upward flux density to $\pi B_\nu(T_c)$ when the surface emission contribution is removed in the transfer calculations, as a function of the vertical optical thickness. The cloud emissivity was found to be independent of the cloud temperature. The emissivity values of cubic clouds are much lower than the plane-parallel values having a maximum difference on the order of 30%. It should be noted that the plane-parallel values were obtained from the discrete-ordinates method (Liou, 1973). For rectangular clouds having a horizontal optical depth 10 times larger than the vertical optical depth, we found that the emissivity values are very close to but larger than the plane-parallel values. The larger emissivities, which approach unity but are not exactly equal to unity, found at the top of a rectangular cloud with optical depths of about (10, 100, 100) as compared with the plane-parallel values are due to approximations employed in the finite cloud analysis. There is also emission from the side surfaces of a rectangular cloud. Its values are much smaller than those from the top surface by as much as 5–10%. The reduction of the emissivity values due to the finite size of the cloud is more evidenced from a cubic cloud. For an optically thick cubic cloud with optical depths of 20, 20 and 20, the emissivity value only approaches to about 0.9 revealing its non-blackness nature. This finding suggests that finite clouds cannot be considered as blackbodies even when they grow to considerable depths in the vertical directions. The inference of the cloud top temperature from the 10 μm window for well-developed cumulus clouds will give a higher value if the cloud emissivity is not properly taken into account.

Although the net flux divergence and infrared cooling rate within clouds assumed to be plane-parallel have been studied comprehensively, effects of the finite dimension on these radiation parameters have not been explored previously. In general, the heating or cooling rate within a finite cloud is a function of the position in the vertical as well as the horizontal directions. In order to have a reasonable comparison with the plane-parallel values, we first evaluate the cooling rate due to the vertical net flux divergence defined by

$$\frac{\partial T}{\partial t} = \frac{\beta_e}{C_p \rho} \frac{\partial \bar{F}_N(\tau_z)}{\partial \tau_z},$$

where β_e denotes the extinction coefficient, C_p the specific heat at constant pressure, ρ the air density, and $\bar{F}_N$ the average net flux density at a given τ_z plane. The differentiation of $\bar{F}_N$ with respect to τ_z can be carried out analytically and therefore a relatively simple expression for the infrared cooling rate may be derived. Fig. 7 illustrates a plot of the infrared cooling rate as a function of height within a cumulus cloud having a typical extinction coefficient of 11 km^{-1} for cloud temperatures of -10 and 0°C. The cloud base experiences positive flux divergence due to the greenhouse effect, whereas the cloud top undergoes strong cooling caused by the cooling to space effect. The much stronger cooling at the top of cubic and rectangular clouds is caused by the cooling to space from the top as well as side walls. The vertical cooling rate difference between the cubic and plane-parallel clouds for the two temperatures employed is on the order of 0.1°C h^{-1}. It should be noted that the heating and cooling of infrared radiation generated within clouds are caused by the adsorption of cloud particles and the subsequent emission of these particles in the corresponding infrared region due to the cloud temperature. Scattering also plays a role in redistributing the heating and cooling within the cloud.

Moreover, we also investigate the averaged cooling rate in the horizontal plane due to the vertical as well as horizontal flux divergence defined in the form

$$\frac{\partial T}{\partial t} = \frac{\beta_e}{C_p \rho} \overline{\nabla \cdot \mathbf{F}_N},$$

where the bar denotes the averaging over the horizontal plane (τ_z surface) and $\mathbf{F}_N$ is a function of τ_x, τ_y and τ_z. For a rectangular cloud, the heating experienced in the cloud bottom is reduced because of the increasing outward horizontal flux to the side surfaces of a finite cloud. The effect of the side leakage is more evidenced when a cubic cloud is employed in the calculations. In reference to the diagram depicted in Fig. 7, the horizontal outward

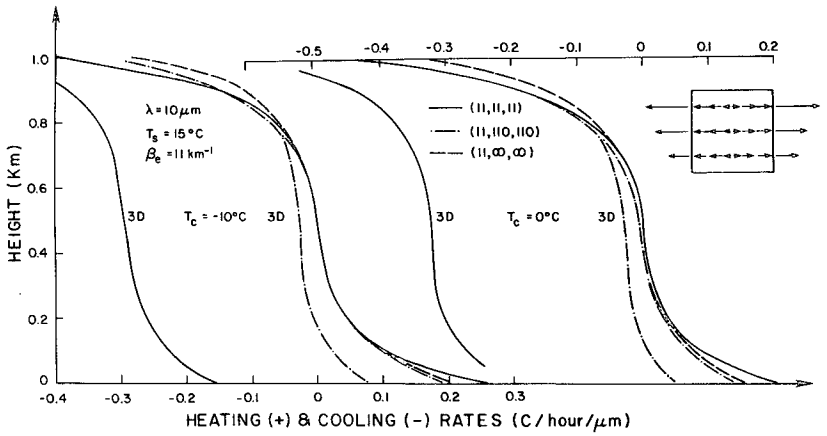

FIG. 7. Vertical infrared cooling rates (°C h^{-1} μm^{-1}) as functions of the height within the cloud having an extinction coefficient of 11 km^{-1} for various cloud models and cloud temperatures. The curves marked with 3D are obtained from the three-dimensional flux density divergence averaged over the horizontal plane. The diagram in the upper right denotes the directions of the horizontal flux density.

flux increases toward the side walls. This increase is particularly enhanced at the cloud top but reduces somewhat near the cloud base. Consequently, a strong cooling at the top is shown, and the cubic cloud bottom also experiences cooling but at a much smaller rate than the top portion.

5. Conclusions

In this paper analytic solutions to the infrared radiative transfer in three-dimensional finite cloud layers are presented. The analyses are based on the four-terms spherical-harmonics expansion for the phase function and intensity in which the surface emission contribution is included. Computations are carried out to investigate the effect of the cloud finite horizontal dimension on the upward and downward intensity and flux density as well as on the cloud emissivity and infrared cooling rates.

A number of highlights of the resulting computations are summarized below:

1) Values of the upwelling intensity from optically thick finite clouds have a maximum at the center of the cloud and they decrease in general toward the cloud edge. The average upward intensities in the upwelling directions are found to be larger for finite clouds than plane-parallel clouds. The average downward intensities for cubic clouds are shown to be smaller than those for rectangular and plane-parallel clouds.

2) The downward flux densities for cubic clouds are smaller as compared to those for rectangular and plane-parallel clouds. However, the upward flux densities of cubic clouds may be greater or smaller than those of rectangular and plane-parallel clouds depending on the cloud temperature.

3) Optically thick cubic clouds may not be considered as black clouds because their emissivity values only approach to about 0.9. The emissivities of cubic clouds are much lower than the plane-parallel values with differences on the order of 20–30%.

4) Near the bottom portions cubic clouds experience larger positive vertical flux density divergence than plane-parallel clouds. When the horizontal component of the flux density divergence is included in the calculations, small cooling takes place near the cubic cloud bottom. The top portions of cubic clouds undergo much stronger cooling as compared to plane-parallel clouds.

Point number (3) has implication to the interpretation of the cloud top temperature for cumulus clouds from satellite soundings. Point number (4) reveals some importance of the cloud horizontal dimension in conjunction with the understanding of infrared cooling in an atmosphere containing cumulus clouds.

Acknowledgments. This research was supported in part by the Atmospheric Research Section of the National Science Foundation under Grants ATM75-05216 and ATM78-26259, and by the Air Force Geophysics Laboratory of the Air Force Systems Command under Contract F-19628-78-C-0144.

REFERENCES

Berg, P. W., and J. L. McGregor, 1966: *Elementary Partial Differential Equations*. Holden-Day, Inc., 421 pp.

Case, K. M., and P. F. Zweifel, 1967: *Linear Transport Theory*. Addison-Wesley, 342 pp.

Chandrasekhar, S., 1950: *Radiative Transfer*. Dover, 393 pp.

Davies, R., 1978: The effect of finite geometry on the three-dimensional transfer of solar irradiance in clouds. *J. Atmos. Sci.*, **35**, 1712–1725.

Greenspan, H., C. N. Kilber and T. Okrent, 1968: *Computing Methods in Reactor Physics*. Gordon and Breach, 589 pp.

Joseph, J. H., W. J. Wiscombe and J. A. Weinman, 1976: The Delta-Eddington approximation for radiative flux transfer. *J. Atmos. Sci.*, **33**, 2452–2459.

Liou, K. N., 1973: A numerical experiment on Chandrasekhar's discrete-ordinate method for radiative transfer: Applications to cloudy and hazy atmospheres. *J. Atmos. Sci.*, **30**, 1303–1326.

——, 1976: On the absorption, reflection and transmission of solar radiation in cloudy atmospheres. *J. Atmos. Sci.*, **33**, 798–805.

McKee, T. B., and S. K. Cox, 1976: Simulated radiance patterns for finite cubic clouds. *J. Atmos. Sci.*, **33**, 2014–2020.

Reynolds, D. W., T. B. McKee and E. S. Danielson, 1978: Effects of cloud size and cloud particles on satellite-observed reflected brightness. *J. Atmos. Sci.*, **35**, 160–166.

Weinman, J. A., and P. N. Swarztrauber, 1968: Albedo of a striated medium of isotropically scattering particles. *J. Atmos. Sci.*, **25**, 497–501.

——, and R. Davies, 1978: Thermal microwave radiances from horizontally finite clouds of hydrometeors. *J. Geophys. Res.*, **83**, 3099–3107.